

In Situ Thickness Assessment During Ion Milling of a Free-Standing Membrane Using Transmission Helium Ion Microscopy

Adam R. Hall*

Joint School of Nanoscience and Nanoengineering, Department of Nanoscience, University of North Carolina Greensboro, Greensboro, NC 27401, USA

Abstract: We describe a novel method for *in situ* measurement of the local thickness of a freely suspended solid-state membrane after thinning with a focused helium ion beam. The technique utilizes a custom stage for the helium ion microscope that allows the secondary electron detector used for normal imaging to collect information from ions transmitted through the sample. We find that relative brightness in the transmission image scales directly with the membrane thickness as determined by atomic force microscopy measurements.

Key words: helium ion microscope, ion milling, silicon nitride membrane, thinning, transmission imaging, STIM

INTRODUCTION

In ion milling, accelerated ions in the primary beam transfer momentum to the target atoms and dislodge them in a controlled manner through the sputtering process. Typically performed with Ga⁺ ions, this technology is used frequently in top-down micro- and nanofabrication, producing a wide range of devices including fluidic systems (Cannon et al., 2004; Menard & Ramsey, 2011) and custom scanning probes (Vasile et al., 1991; Menozzi et al., 2005), as well as electron-transparent samples for transmission electron microscopy (Giannuzzi et al., 1998; Giannuzzi & Stevie, 1999; Mayer et al., 2007).

Recent advances have allowed the development of the helium ion microscope (HIM), an instrument capable of producing a bright, coherent beam of He⁺ ions from an atomically sharp source (Ward et al., 2006). The HIM has shown wide utility in microscopy, including dopant profiling (Jepson et al., 2009, 2011) and imaging of uncoated biological material (Scipioni et al., 2009; Bazou et al., 2011), but the use of He⁺ also has distinct advantages over Ga⁺ in terms of fabrication. The most significant among these is the relatively low mass of He⁺, which results in less damage per ion. This lower milling yield makes the milling process more controllable and precise—an effect that has been demonstrated, for example, through milling of graphene (Bell et al., 2009; Lemme et al., 2009) and through fabrication of nanopore devices below 5 nm in diameter (Yang et al., 2011).

We demonstrated recently that the HIM beam can be used to reduce the local thickness of a free-standing membrane of silicon nitride (SiN) controllably by exposing it to predetermined amounts of ion dose (Marshall et al., 2012). However, in this previous work, resultant membrane thickness was determined *ex situ* using topographic measurements of the SiN with atomic force microscopy (AFM). This procedure is lengthy, does not easily permit repeated

exposure-measurement cycles, and may induce additional contamination on the sample surface. In the present work, we show that local film thickness can be determined instead through direct imaging of the membrane *in situ* using a scanning transmission ion microscopy (STIM) stage in the HIM. By quantifying the brightness of a thinned region relative to the native membrane around it, a measure of local thickness can be obtained. We use AFM measurements to support these measurements and we justify the observed trend through TRIM modeling

MATERIALS

Low-stress SiN membranes supported by 200- μ m-thick silicon frames were obtained commercially (Norcada Inc., Edmonton, Canada). Ellipsometry measurements of the SiN film revealed a thickness of 24.5 nm.

Ion milling and characterization of freely suspended membranes was carried out in the imaging chamber of a HIM (Orion PLUS, Zeiss, Thornwood, NY, USA), with samples mounted on a custom STIM stage (Fig. 1a). On this stage, a single chip can be positioned with the SiN membrane above an open cylinder with length of \sim 8 mm. At the bottom of this path is a beam-limiting aperture of \sim 1 mm followed directly by an angled surface of polished metal with a gold coating. The overhang of the sample plate is such that it does not occlude the path of secondary electrons produced at the polished metal surface from reaching the detector that is used commonly for imaging in the instrument (Fig. 2b). In this way, pixel-by-pixel information can be collected from transmitted He⁺ ions without the need for an additional detector positioned in the beam path below the sample.

EXPERIMENTAL

HIM Milling Procedure

Directly before processing, a sample was cleaned with an oxygen plasma of 150 W for 2 min and then loaded onto

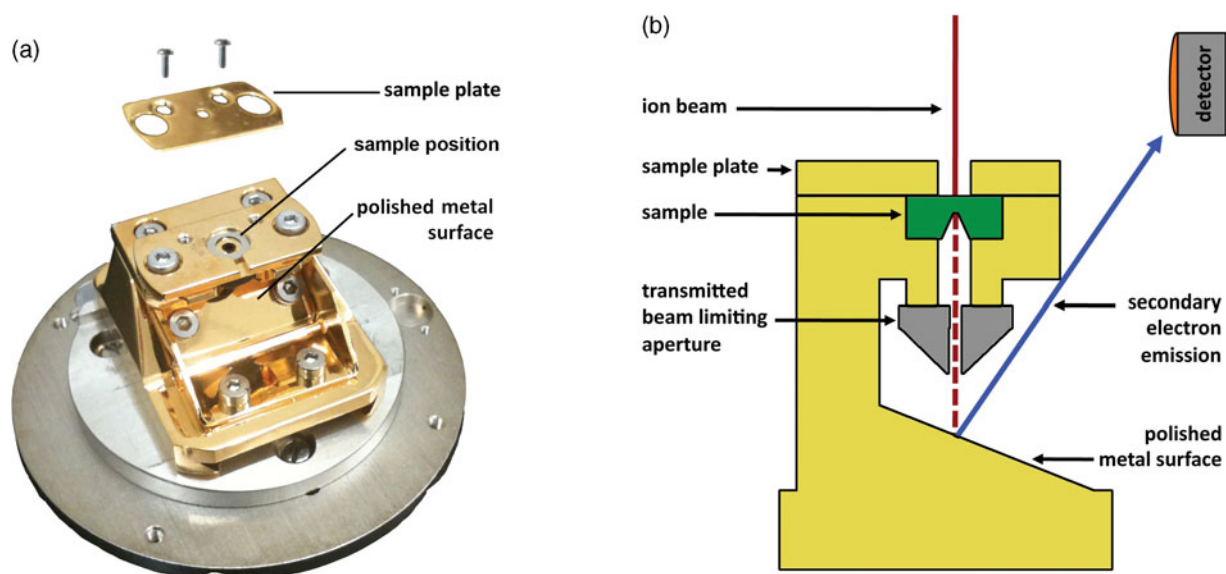


Figure 1. Helium ion microscope transmission imaging stage. **a:** Photograph of the custom transmission stage sample holder. **b:** A schematic showing the sample (green) suspended above a narrow opening leading to a polished metal surface. He⁺ ions that are able to transmit through the sample with little to no deflection (bright field) interact with the metal surface, producing secondary electrons that can be measured by the Everhart–Thornley detector above.

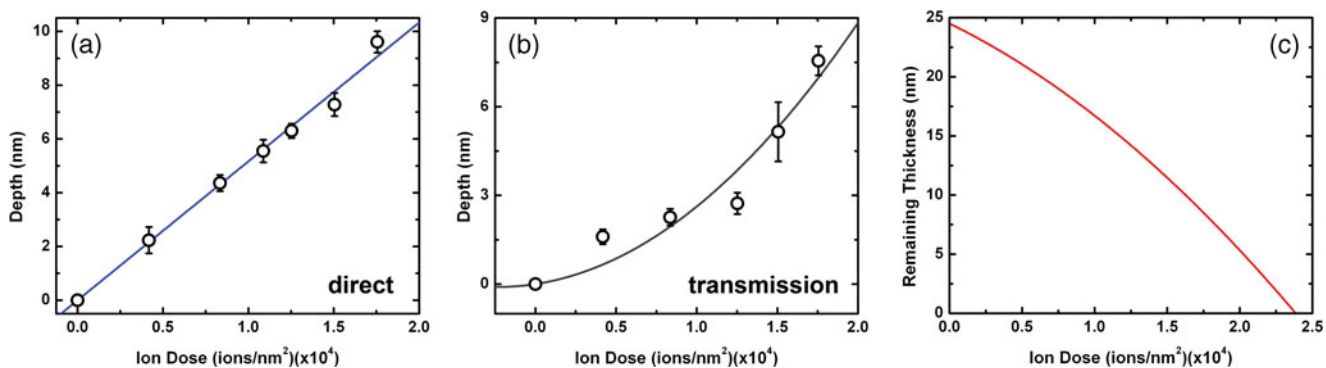


Figure 2. Atomic force microscopy depth measurements of direct and transmission helium ion microscope milling. Depth of 500-nm square patterns milled with various ion doses in a suspended 24.5-nm-thick silicon nitride (SiN) membrane as measured directly by atomic force microscopy. Shown are measurements of direct (membrane surface of ion incidence, **a**) and transmission (membrane surface opposite of ion incidence, **b**) milling. **c:** The calculated remaining thickness of a SiN membrane versus dose, using the fits from **(a)** and **(b)**.

the STIM stage, either with the flat side of the chip facing up (direct milling) or facing down (transmission milling). After introducing the STIM holder into the sample exchange chamber, an additional cleaning step was performed using an integrated air plasma cleaner (10 W for 3 min) to remove any additional contamination deposited on the sample during loading.

After insertion into the imaging chamber, the STIM holder was positioned to a working distance of ~ 6 mm and rotated such that the polished metal surface was oriented toward the secondary electron detector. These conditions permit STIM imaging by creating an unobstructed path from the polished surface to the detector. The ion beam current was set to a value of 5.1 pA (35 kV accelerating voltage) through a 20- μ m aperture by adjusting the condenser lens and the helium pressure. Directly before perform-

ing milling, the beam was optimized at a position close to the SiN membrane on the supporting chip. Because the cleaned substrate surface had no features to use for this optimization, a single milled spot was formed by exposing the ion beam at one location for ~ 10 s. The resultant circular feature (~ 200 nm in diameter) was then used to fix stigmatism and focus. The probe size of the resulting beam is < 1 nm (Scipioni et al., 2008). Once adjusted satisfactorily, a bias of ~ 40 V was applied directly to the sample holder in order to suppress secondary electron signal from the top sample surface. The beam was then blanked and the sample was moved to position the SiN window in the beam path. There, exposure of single square patterns was performed under computer control. 500×500 nm regions were milled for AFM analysis in order to ensure that the floor of the patterned region could be imaged by the probe, whereas

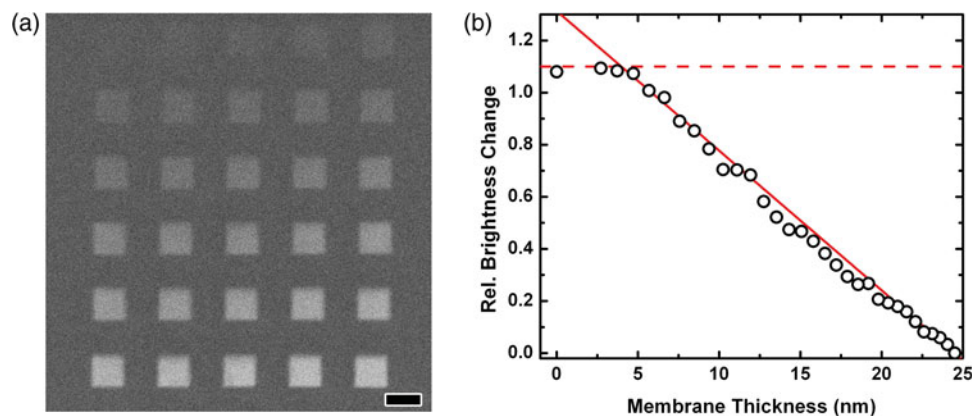


Figure 3. Transmission He⁺ ion imaging of a locally thinned silicon nitride (SiN) membrane. **a:** Scanning transmission ion micrograph of an array of 100-nm squares milled in a 24.5-nm-thick SiN membrane. Total He⁺ ion dose ranges from 6.8×10^2 ions/nm² (top left) to 2.0×10^4 ions/nm² (lower right). Scale bar is 100 nm. **b:** Correlation between brightness change of the square-patterned regions in a transmission helium ion microscope image and SiN membrane thickness. Brightness change is measured relative to the native membrane, and SiN thickness is taken from the relation in Figure 2c. The solid line is a linear fit to the data and the dashed line represents the apparent contrast limit.

100 × 100 nm regions were milled for STIM imaging. The base pattern used a pixel dwell time of 0.1 μs, resulting in a dose of 687 ions/nm². Subsequent regions were milled after moving the membrane a lateral distance at least twice the size of the square pattern in order to minimize the effects of surface charge accumulation on the milling process (Marshall et al., 2012). Repetition of the base pattern exposure at the same location was used to create milled regions with higher total dose. This was found to prevent structural deformities caused by sample charging and redeposition of milled material (Santamore et al., 1997), resulting in a patterned region with a smooth, constant depth.

Patterned regions intended for AFM inspection were not imaged with the HIM following their fabrication. For samples that were imaged *in situ* with the STIM stage, image acquisition was performed using a pixel dwell time of no more than 5 μs and with a field of view of 1–3 μm. Under these conditions, the total dose during imaging did not exceed 80 ions/nm² and therefore did not cause appreciable milling of the sample during the image scan. The average pixel brightness within the milled squares and on the surrounding native membrane was measured using ImageJ (Abramoff et al., 2004). Data were normalized by considering relative brightness change, $(B_p - B_o)/B_o$, where B_p is average brightness within the patterned region and B_o is average brightness of the native membrane.

AFM Measurements

AFM images of each milled square were collected using an Agilent 5600LS (Agilent Technologies, Englewood, CO, USA) operating in tapping mode. NanoWorld Arrow noncontact tips were used, with a typical radius of curvature of <10 nm at the tip. Average milling depth for each ion dose in both direct and transmission milling was determined by comparing the average height within the patterned region to that of the unmilled membrane at a distance such that the membrane surface was planar. This removed potential artifacts

that could be caused by local membrane deformation directly around the milled regions. The AFM tip was able to reach the bottom surface of the 500-nm trenches in all instances. Measurement error stems from the surface roughness across the measured regions.

RESULTS AND DISCUSSION

AFM inspection of a series of 500 × 500 nm milled squares was performed in order to determine the relationship between incident ion dose and remnant membrane thickness. Measurements were completed using the convention established previously (Marshall et al., 2012). First milling was performed with the ion beam incident on the front face of the sample chip and AFM data taken on the same side. Then, milling was performed with the ion beam incident on the back face of the sample chip, but with AFM data again taken on the front face. In this way, we were able to obtain topographical images both of the side of ion incidence (“direct” milling) and of the side opposite of ion incidence (“transmission” milling). The average depths of patterned regions made using multiple ion doses in both milling modes are plotted in Figures 2a and 2b, respectively. We find that direct-milling depth varies linearly with ion dose, whereas transmission-milling depth varies with the square of the ion dose, in agreement with the relationship measured previously for thicker membranes. Using the fits to these data and knowing the original membrane thickness, a relationship between ion dose and remaining membrane thickness can be determined easily (Fig. 2c).

Having determined the expected membrane thickness for a range of ion exposures, we next repeated the milling procedure on a new chip for STIM analysis. Here, a regular array of 100 × 100 nm squares was produced with varying ion doses before a single image of the entire array was obtained (Fig. 3a). Qualitatively, the resultant image shows that regions exposed with a higher ion dose are brighter, in

agreement with our previous findings. In order to quantify this behavior more fully, we next compared the brightness within each successive milled region with the brightness of the unmilled membrane and plotted the values against the local membrane thickness in each square, as determined by the dependence in Figure 2c. The results show that STIM image brightness correlates directly with membrane thickness (Fig. 3b). We find that the relative brightness change breaks from this linear relationship for very low thickness. This may be due to saturation of the detector or an inability to resolve very small amounts of ion deflection from the original beam. Even taking this into account, *in situ* measurement of the brightness can be used to determine local membrane thickness down to about 5 nm.

The pixel brightness determined by an Everhart–Thornley secondary electron detector (Everhart & Thornley, 1960)—such as the one used in the HIM—correlates with incident electron count under normal conditions (Seah, 1990). For this reason, we can assume that the brightness results described above indicate that the total number of He⁺ ions transmitted through the SiN membrane and arriving at the polished metal surface varies directly with membrane thickness. This assumes that the average secondary electron emission per primary ion at the metal surface is a constant (Lai et al., 1986; Ramachandra et al., 2009). Because the STIM holder used in the experimental measurements includes a beam-limiting aperture between the sample and the metal surface, we postulated that the number of primary ions contributing to the secondary electron image was dependent on the scattering angle. He⁺ ions that transmitted through the SiN membrane but exited at a sufficiently large angle relative to the beam axis will be stopped by the aperture and thus not contribute to the image.

In order to investigate the phenomenon further, we modeled the transmission of He⁺ ions through SiN membranes of various thicknesses using TRIM software. Using freely available software (Zeigler et al., 1985), a model was created to represent the unmodified SiN membrane. The input thickness was 24.5 nm, to match the value determined experimentally through ellipsometry, and the stoichiometry was set at a ratio of 3:4 (Si:N). Ion–atom interactions were calculated for a total of 10,000 incident He⁺ ions in a beam of 35 keV, set to match the value used in experiments. For each transmitted ion, the final trajectory was calculated to determine the amount of deflection caused by interactions with membrane atoms. This procedure was repeated using the same conditions, but with an initial input membrane thickness of 18, 12, 7, and 2 nm, respectively.

The resulting trajectory data showed a linear increase in the total number of transmitted ions, with direction vectors falling below a threshold angle as the membrane thickness was decreased. In Figure 4, data are displayed for three discrete threshold angles (0.1, 0.15, and 0.25 rad, respectively), each showing the linear variation and converging at zero thickness where no ion paths are deflected. These results support our explanation of the experimental data and why STIM image brightness can be used as a direct

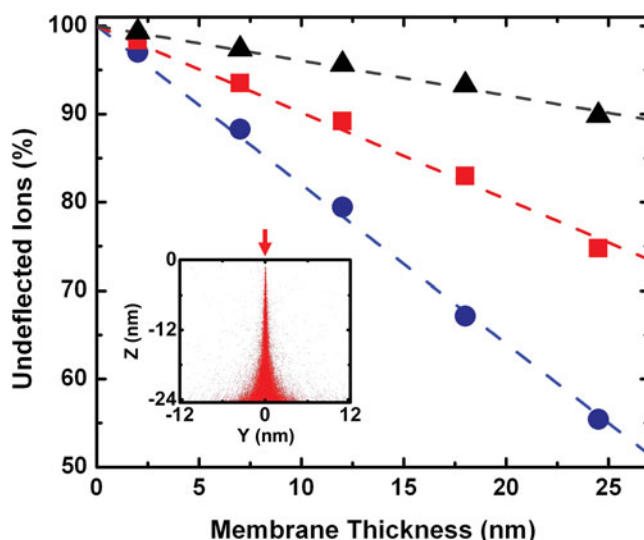


Figure 4. TRIM modeling of He⁺ ion transmission through thinned silicon nitride (SiN) membranes. Percentage of He⁺ ions transmitted through a SiN membrane of varying thickness, such that the transmitted ion direction is altered less than a threshold value of 0.1 (blue circles), 0.15 (red squares), and 0.25 (black triangles) radians from normal incidence. The first of these represents the estimated cutoff angle of the scanning transmission ion microscopy holder used in these experiments. For each membrane thickness considered, a new TRIM model was constructed and data on the ions ($n = 10,000$) transmitted through the membrane were analyzed. Inset: Calculated scattering profile of He⁺ ions through a 24.5-nm SiN membrane. The red arrow indicates point of incidence.

measure of membrane thickness. They also indicate that the use of a narrower aperture in the STIM holder may result in an increase in sensitivity, as the same change in membrane thickness would yield a larger change in brightness. This may be an additional route to measurement below 5-nm thicknesses.

CONCLUSIONS

We have demonstrated that local thickness variations in a thin suspended membrane can be quantified *in situ*. We performed HIM milling with various total ion doses on a SiN membrane and imaged the resulting patterned regions using a custom STIM stage. Using parallel topographical data taken with AFM, we showed that secondary electron image brightness varies linearly with membrane thickness. With present limitations, this technique can be used to measure membrane thickness down to about 5 nm. We presume that the upper limit of thickness will be determined by the limit of detectable ion transmission through the membrane. We used TRIM modeling to show that the percentage of transmitted ions with a direction vector that is deflected less than a threshold angle from the original beam path increases linearly with decreasing SiN membrane thickness. This supports the notion that primary ions transmitting through thicker membrane sections will be scattered more strongly on average and be stopped by the

beam-limiting aperture of the holder, thus not contributing to image formation. As the observed brightness change is caused by scattering of the ion beam, and thus by a material property of the thin membrane, this method of *in situ* thickness determination should be applicable to a wide range of monolithic materials in addition to SiN. We note that a calibration of membrane thickness to brightness would be expected to hold only for a given setting of image contrast and brightness. However, this is easily set in the HIM.

There may be applicability of the method in conventional Ga⁺ ion milling, although we expect controllability to be severely reduced compared with He⁺. We expect that the described method will have direct impact on device fabrication schemes in which control over membrane thickness is advantageous, including nanoelectromechanical resonators (Adiga et al., 2012) and solid-state nanopores (Wanunu et al., 2010).

ACKNOWLEDGMENTS

We gratefully acknowledge L. Stern for the custom STIM holder used in these experiments. We thank L. Stern and J. Yang for helpful discussions and S. Iyer for ellipsometry measurements of membrane thickness. This research was funded by the North Carolina Biotechnology Center through Biotechnology Research Grant #2011-BRG-1201.

REFERENCES

- ABRAMOFF, M.D., MAGALHAES, P.J. & RAM, S.J. (2004). Image processing with ImageJ. *Biophotonics Int* **11**(7), 36–42.
- ADIGA, V.P., ILIC, B., BARTON, R.A., WISON-RAE, I., CRAIGHEAD, H.G. & PARPIA, J.M. (2012). Approaching intrinsic performance in ultra-thin silicon nitride drum resonators. *J Appl Phys* **112**(6), 064323.
- BAZOU, D., BEHAN, G., REID, C., BOLAND, J.J. & ZHANG, H.Z. (2011). Imaging of human colon cancer cells using He-ion scanning microscopy. *J Microsc* **242**(3), 290–294.
- BELL, D.C., LEMME, M.C., STERN, L.A., WILLIAMS, J. R. & MARCUS, C.M. (2009). Precision cutting and patterning of graphene with helium ions. *Nanotechnology* **20**(45), 455301.
- CANNON, D.M., FLACHSBART, B.R., SHANNON, M.A., SWEEDLER, J.V. & BOHN, P.W. (2004). Fabrication of single nanofluidic channels in poly(methylmethacrylate) films via focused-ion beam milling for use as molecular gates. *Appl Phys Lett* **85**(7), 1241–1243.
- EVERHART, T.E. & THORNLEY, R.F.M. (1960). Wide-band detector for micro-microampere low-energy electron currents. *J Sci Instrum* **37**(7), 246–248.
- GIANNUZZI, L.A., DROWN, J.L., BROWN, S.R., IRWIN, R.B. & STEVIE, F. (1998). Applications of the FIB lift-out technique for TEM specimen preparation. *Microsc Res Tech* **41**(4), 285–290.
- GIANNUZZI, L.A. & STEVIE, F.A. (1999). A review of focused ion beam milling techniques for TEM specimen preparation. *Micron* **30**(3), 197–204.
- JEPSON, M., LIU, X., BELL, D., FERRANTI, D., INKSON, B. & RODENBURG, C. (2011). Resolution limits of secondary electron dopant contrast in helium ion and scanning electron microscopy. *Microsc Microanal* **17**(4), 637–642.
- JEPSON, M.A.E., INKSON, B.J., LIU, X., SCIPIONI, L. & RODENBURG, C. (2009). Quantitative dopant contrast in the helium ion microscope. *Europhys Lett* **86**(2), 26005.
- LAI, S.Y., BRIGGS, D., BROWN, A. & VICKERMAN, J.C. (1986). The relationship between electron and ion induced secondary-electron imaging—A review with new experimental observations. *Surf Interface Anal* **8**(3), 93–111.
- LEMME, M.C., BELL, D.C., WILLIAMS, J.R., STERN, L.A., BAUGHER, B.W.H., JARILLO-HERRERO, P. & MARCUS, C.M. (2009). Etching of graphene devices with a helium ion beam. *ACS Nano* **3**(9), 2674–2676.
- MARSHALL, M.M., YANG, J. & HALL, A.R. (2012). Direct and transmission milling of suspended silicon nitride membranes with a focused helium ion beam. *Scanning* **34**(2), 101–106.
- MAYER, J., GIANNUZZI, L.A., KAMINO, T. & MICHAEL, J. (2007). TEM sample preparation and FIB-induced damage. *MRS Bull* **32**(5), 400–407.
- MENARD, L.D. & RAMSEY, J.M. (2011). Fabrication of sub-5 nm nanochannels in insulating substrates using focused ion beam milling. *Nano Lett* **11**(2), 512–517.
- MENOZZI, C., GAZZADI, G.C., ALESSANDRINI, A. & FACCI, P. (2005). Focused ion beam-nanomachined probes for improved electric force microscopy. *Ultramicroscopy* **104**(3–4), 220–225.
- RAMACHANDRA, R., GRIFFIN, B. & JOY, D. (2009). A model of secondary electron imaging in the helium ion scanning microscope. *Ultramicroscopy* **109**(6), 748–757.
- SANTAMORE, D., EDINGER, K., ORLOFF, J. & MELNGAILIS, J. (1997). Focused ion beam sputter yield change as a function of scan speed. *J Vac Sci Technol, B* **15**(6), 2346–2349.
- SCIPIONI, L., ALKEMADE, P., SIDORKIN, V., CHEN, P., MAAS, D. & VAN VELDHOVEN, E. (2009). The helium ion microscope: Advances in technology and applications. *Am Lab* **41**(12), 26–28.
- SCIPIONI, L., STERN, L.A., NOTTE, J., SIJBRANDIJ, S. & GRIFFIN, B. (2008). Helium ion microscope. *Adv Mater Process* **166**(6), 27–30.
- SEAH, M.P. (1990). Channel electron multipliers: Quantitative intensity measurement—efficiency, gain, linearity and bias effects. *J Electron Spectros Relat Phenomena* **50**(1–2), 137–157.
- VASILE, M.J., GRIGG, D., GRIFFITH, J.E., FITZGERALD, E. & RUSSELL, P.E. (1991). Scanning probe tip geometry optimized for metrology by focused ion beam milling. *J Vac Sci Technol B* **9**(6), 3569–3572.
- WANUNU, M., DADOSH, T., RAY, V., JIN, J., McREYNOLDS, L. & DRNDIC, M. (2010). Rapid electronic detection of probe-specific micRNAs using thin nanopore sensors. *Nat Nanotechnol* **5**(11), 807–814.
- WARD, B.W., NOTTE, J.A. & ECONOMOU, N.P. (2006). Helium ion microscope: A new tool for nanoscale microscopy and metrology. *J Vac Sci Technol, B* **24**(6), 2871–2874.
- YANG, J., FERRANTI, D.C., STERN, L.A., SANFORD, C.A., HUANG, J., REN, Z., QIN, L.-C. & HALL, A.R. (2011). Rapid and precise scanning helium ion microscope milling of solid-state nanopores for biomolecule detection. *Nanotechnology* **22**(28), 285310.
- ZEIGLER, J., BIRSACK, J. & LITTMARK, U. (1985). *The Stopping Range of Ions in Matter*. New York: Pergamon Press. Available at <http://www.srim.org>.